Eleventh International Conference on Computational Fluid Dynamics (ICCFD11), Maui, HI, USA 2022

ICCFD11-2022-0901

Propeller Representation in Full-Vehicle CFD: Actuator Disk Versus Body-Force Modeling Approaches

Tianbo Xie*, and Alejandra Uranga*
Corresponding author: auranga@usc.edu

*University of Southern California, Los Angeles, CA 90089, U.S.A.

Abstract: This paper presents the application of a body-force propulsor model to represent propellers in RANS simulations and accurately capture aero-propulsive coupling effects. The model utilizes a source field to mimic the effect of turning blades on the passing flow, including work input and viscous losses. With only the blade geometry and rotational speed as input, it requires no empirical data and takes the local flow into account to provide a realistic response. The model is applied to the simulation of a case with strong propeller-airframe interactions, namely a blown-lift wing in which distributed propellers blow onto a flapped-wing to produce high lift. Results are compared with an advanced actuator disk model and with experimental measurements. We look at the load distribution, propeller performance, jet properties, and wing performance for a range of operating conditions. For an isolated propeller, both body-force and actuator disk models make comparable flow-field predictions. However, the former is able to predict propeller performance (thrust, power, efficiency) and match experimental data with only the wheel speed specified, while the latter requires the thrust as an input and does not predict efficiency. In the blown-lift application, the body-force model is found to successfully predict wing-propeller interactions, and responds to the local flow in a way that better mimics actual propeller operation.

Keywords: Propeller Modeling, Body-Force Model, Actuator Disk, Blown-Lift, Aerodynamics, Computational Fluid Dynamics.

Nomenclature

b = Blockage factor
B = Number of blades
C_{p_t} = Total pressure coefficient
C_p = Pressure coefficient
c_T = Thrust coefficient
c_P = Power coefficient
e_t = Specific total energy
h_t = Specific total enthalpy
K_c = Compressibility correction factor
$\hat{\mathbf{n}}$ = Normal unit vector to blade camber
p = Static pressure
p_t = Total pressure
r = Radial location
R = Propeller tip radius
$\mathcal{R}$ = Standard air gas constant
s = Specific entropy
t = Blade thickness
T = Thrust
$\mathbf{U}$ = Blade velocity vector
$\mathbf{V}$ = Absolute flow velocity vector
$\mathbf{W}$ = Relative flow velocity vector
x = Axial location
α = Absolute swirl angle; or angle of attack
δ = Local deviation angle
δ_f = Flap deflection angle
η = Aerodynamic efficiency
γ = Air specific heat ratio
κ = Blade section stagger angle
λ = Advance ratio
θ = Circumferential location
ρ = Density
$\bar{\bar{\tau}}$ = Viscous stress tensor
$(\,)_{\text{ref}}$ = Reference quantity
$(\,)_x$ = Axial component
$(\,)_i$ = Quantity at ith axial station
$(\,)_\theta$ = Circumferential component
$||\cdot||$ = Vector magnitude

1 Introduction

1.1 Motivation

Recent flying vehicle developments have focused on increasing efficiency to reduce emissions and enhance air-mobility for regional and urban markets. This has led to unconventional aircraft concepts with tightly coupled airframe and propulsion systems. In these designs, strong interactions between the airframe and the propulsors, known as aero-propulsive coupling, are utilized to bring extra benefits or vehicular capabilities. One example is the use of boundary layer ingesting (BLI) engines, in which part of the airframe boundary layer gets ingested by the propulsors in order to reduce the required power. This idea was adopted in several conceptual aircraft designs [1, 3] and was theoretically proven to bring system level benefits for the D8 aircraft [2, 4]. Another example is the use of blown-lift technology in which a wing-mounted distributed electric propulsion (DEP) system produces a jet sheet blowing over a flapped wing. Very high lift levels can then be produced via the synergetic interaction between DEP and airframe, and be leveraged to enable ultra short take-off and landing (STOL) vehicles.

Along with the many benefits brought by the aero-propulsive coupling effects, the interaction poses a new challenge to the design of such aircraft, more specifically the accurate modeling of complex interactions between the propulsor system and airframe in high-fidelity full aircraft CFD. As a result, advanced propulsor models are needed for these novel vehicles in order to accurately capture the coupling effect and its influence on system performance.

This paper builds upon a body-force propulsor model originally developed to represent ducted fan type propulsors and validated against experimental data for high-speed and low-speed fan stages [5, 6]. The adaptation of that body force model to better represent propellers is presented in this paper, and applied to a simplified blown-lift geometry for STOL applications as part of a collaborative project with Electra.aero funded under a NASA STTR program.

1.2 Propulsor Modeling

The most common type of propulsor model used in high-fidelity aircraft CFD simulations is the actuator disk model which imposes a prescribed pressure jump or load distribution. Actuator disks can generally adequately represent isolated propulsors but have some inherent deficiencies. First, they require empirical inputs, such as the propeller characteristic, to specify the loading at certain operating point. Thus the propeller performance needs to be known *a priori*. Second, the load distribution is prescribed and fixed, and thus won't properly respond to any flow condition variations. This is the main reason why actuator disk models are unlikely to be sufficient for representing propulsors with strong aero-propulsive coupling. The propulsors may operate under non-uniform flow or partially off-design conditions in the presence of the airframe's influence. The airframe flow and performance may also be affected by the propulsor's response, and needs to be captured by the model.

In order to better capture the aero-propulsive coupling, we adopt a more advanced body-force model that uses propulsor information, including the propeller blade camber surface geometry, thickness distribution, and rotational speed, together with local flow conditions such as density, velocity and flow directions to produce a force field that mimics the pitch-averaged effects of the turning propeller blades. The force field is implemented as a source term in the governing equations. By taking the flow conditions into account, the body-force model is capable of interacting with and producing a response appropriate to the local flow non-uniformities. In addition, this model requires no empirical input such as pre-computed loadings or pressure rise. As such, this model is expected to be a more realistic representation for propulsors in situations with strong aero-propulsive coupling.

The body-force approach adopted in this work was originally introduced by Marble [7] for turbomachinery applications, and further developed with a more physics-based analytical formulation by Gong [8] who implemented the model in a three-dimensional Euler solver. Gong's formulation represents the blade response to local deviations in flow angle relative to the blade camberline, and is thus capable of responding to local flow distortion. The main disadvantage of his formulation is that it requires blade-specific empirical calibration based on data from measurements or full-wheel CFD computations.

More recently, Hall [9] reformulated a body-force model based on local flow variables, thus eliminating the need for calibration or empirical input, and showed good prediction of inviscid redistribution effects in

a BLI propulsor. In our previous work [5], Hall's inviscid formulation was expanded to viscous compressible computations by incorporating a compressibility correction, and blade metal blockage modeling, together with viscous loss terms in order to predict propulsor efficiency and better represent off-design operation. The model was validated against experimental data for high speed [5] and low speed [6] turbomachinery applications.

1.3 Scope

The objectives of this work are to: (1) extend our body-force model to propeller applications; (2) validate the model predictions for isolated propellers against experimental data; and (3) compare predictions from the body-force model with those from an advanced actuator disk model in both an isolated setup and in a blown-lift wing configuration. We aim to determine whether the more advanced body-force model is required, or the actuator-disk approach (with pressure rise and swirl) is sufficient, to simulate blown-lift wings with distributed electric propulsion (DEP). We pay particular attention to the flow mechanisms affecting the propeller operation in the presence of strong wing-propeller interaction.

This paper is organized as follows. Section 2 presents the methodology, including formulations for both the actuator disk model and the body-force model tested, the blown-lift geometry, and the computational setup. Section 3 examines results for an isolated propeller test cases using the body-force model and compares them against wind tunnel measurements and actuator disk predictions. The blown-lift wing test cases are then shown in Section 4 and the body-force and actuator disks models compared. We examine flow features of the distorted flow upstream of the propulsor, and the flow downstream in order to understand how the propeller performance is affected and whether the propulsor models provide adequate response. Summary and conclusions are given in Section 5.

2 Methodology

2.1 Propeller Models

Two propulsor models are tested in this work to represent propellers, both implemented as source terms in the governing equations. Their formulations are detailed here.

2.1.1 Actuator Disk Model

In this work, we implemented an advanced actuator disk model similar to what is used by [10], which provides more realistic load distribution and flow swirling than just an uniform pressure jump. The actuator disk model specifies a total thrust, T_{spec}, that is radially distributed following Betz optimal circulation distribution with Prandtl's tip correction. Its local force per volume can be generally described as follows

$$\mathbf{f}_{\text{AD}} \;=\; \mathbf{f}_{\text{AD}}(\, r, R, B, T_{\text{spec}}, \lambda \,) \;, \tag{1}$$

where r is the local radius (distance to propeller axis), R the propeller tip radius, B the number of blades and λ the tip advance ratio. Note that the application of this model needs as input the thrust versus advance ratio relation for the specific propeller being represented. For this, we used the c_T-λ information from the wind tunnel experiments (shown in the results section) in order to set the advance ratio when thrust is specified as the input parameter.

The force term $\mathbf{f}_{\text{AD}}$ has axial and tangential components expressed as

$$f_a = \frac{T_{\text{spec}}}{\mathcal{V}}\, K(r) \tag{2}$$

and

$$f_\theta = \frac{T_{\text{spec}}}{\mathcal{V}}\, K(r)\lambda_w(r) \;, \tag{3}$$

respectively, where λ_w is the local wake advance ratio which varies with radial location, K is a scaling factor responsible for distributing the loading, and $\mathcal{V}$ is the total volume of the model region. By assumeing Betz

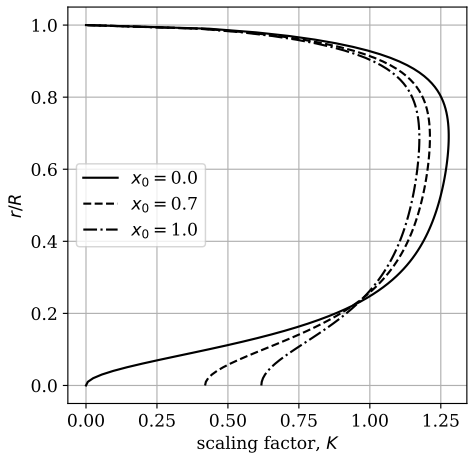

Figure 1: Actuator disk radial load distribution for different x_o constants with $B=4$, $\lambda=0.1$, and $r_{\text{hub}}=0$.

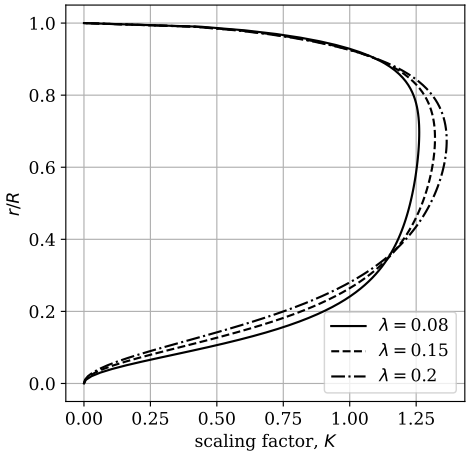

Figure 2: Actuator disk radial load distribution for various advance ratios λ with $B=4$, $x_0=0$, and $r_{\text{hub}}=0$.

optimal circulation distribution and applying Prandtl's tip correction, K takes the form

$$K(r) = \frac{1}{K_c} F(r)\, C_{\Gamma_{\text{Be}}}(r)\ , \tag{4}$$

with the modified non-dimensional form of Betz optimal distribution

$$C_{\Gamma_{\text{Be}}}(r) = \frac{x_0^2 + 1/\lambda_w^2}{1 + 1/\lambda_w^2 + x_0^2}\ , \tag{5}$$

a scaling factor for applying Prandtl's tip correction set to

$$F(r) = \frac{2.0}{\pi} \cos\left(\exp\left(-f\right)\right) \tag{6}$$

where

$$f = \frac{1}{2} B \left(1.0 - \frac{r}{R}\right) \sqrt{1.0 + \frac{1.0}{\lambda_{w_{\text{tip}}}^2}}\ , \tag{7}$$

and the scaling factor

$$K_c = \frac{1}{R - r_{\text{hub}}} \int_{r_{\text{hub}}}^{R} F(r)\, C_{\Gamma_{\text{Be,o}}}(r)\, \mathrm{d}r \tag{8}$$

that ensures the total integrated thrust is the same as the specified value T_{spec}.

The constant x_0 in Equation (5) provides a way to adjust the loading near the center of the propeller. As shown in Figure 1, lower x_0 gives lower loading near the center and vise versa. In this work, we choose $x_0 = 0$ to better compare with the body-force model which generates zero loading at the center. Figure 2 shows the effect of advance ratio on radial load distribution.

2.1.2 Body-Force Model

The body-force modeling approach inherits the idea of turbomachinery through-flow models that aim to create the necessary flow turning instead of directly specifying blade loading. As illustrated in Figure 3, a force field which spans the region swept by the propeller blades is imposed on the passing-through flow to mimic the pitch-averaged effect of the turning blades without actually including the blade surfaces in the

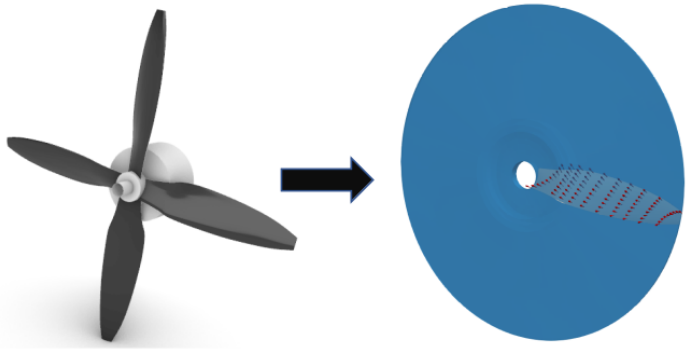

Figure 3: Body-force representation of a propeller: (left) actual propeller geometry, and (right) body-force volume in the computational domain showing camberline normals.

flow domain. The local body-force, *i.e.*, force per unit mass, can be described in general as follows

$$\mathbf{f}_{\mathrm{BF}} \;=\; \mathbf{f}_{\mathrm{BF}}(\,\hat{\mathbf{n}}, B, b, \boldsymbol{\Omega}, \mathbf{V}\,)\;, \tag{9}$$

where $\hat{\mathbf{n}}$ is the local blade camber surface normal, b a flow blockage factor to represent blade thickness, $\boldsymbol{\Omega}$ the wheel rotational velocity and $\mathbf{V}$ the local flow velocity.

In this work, we adopt a form of the body-force model that we previously developed for modeling turbofan-type engines, and which has gone through two previous iterations to better incorporate fundamental physical effects [5, 6]. The formulation used for this paper introduces a slight change to the inviscid loading of previous versions in order to represent the low-solidity, low-blade count, of propellers.

The model formulation can be broken down into three parts corresponding to three major effects, namely the inviscid blade loading, viscous loss (or entropy) generation and metal blockage effects. We briefly introduce the three components of the current model formulation here, together with the modification done for this work. More detailed descriptions and discussions of the formulations can be found in [5, 6].

Inviscid Blade Loading. The inviscid loading force, $\mathbf{f}_n$, is perpendicular to the blade relative flow velocity, $\mathbf{W}$, direction and its magnitude is determined as follows

$$\mathbf{f}_n \;\equiv\; K_c\;\frac{(2\pi\,\delta)\,\left(\frac{1}{2}\mathbf{W}^2\right)}{(2\pi\,r/B)\;b\;|n_\theta|}\;\hat{\mathbf{e}}_n\;, \tag{10}$$

where

$$\hat{\mathbf{e}}_n \;=\; \mathrm{sign}(\mathbf{W}\cdot\hat{\mathbf{n}})\;\frac{\mathbf{W}\times(\mathbf{W}\times\hat{\mathbf{n}})}{||\mathbf{W}\times(\mathbf{W}\times\hat{\mathbf{n}})||}\;, \tag{11}$$

in which $|n_\theta|$ is the circumferential component of the camber normal vector. This force deflects the flow to reduce the local deviation angle, δ, of the local flow relative to the fictitious blade camber surface. The force magnitude is set to scale with the local deviation angle with a factor of 2π analogous to thin airfoil theory's "$c_\ell = 2\pi\alpha$", since this force is the result of a local pressure difference produced by the propeller blades once it is distributed across the blade pitch.

This inviscid loading formulation was originally developed by Hall [9] and modified by [5, 6]. An additional factor of $1/|n_\theta|$ was added to $\mathbf{f}_n$ in our previous model modifications [5, 6] to better predict loading for high solidity turbomachinery applications such as engine fans. This was done following the finding in a potential flow cascade study [11] that blade lift coefficient scales linearly with $1/\cos(\kappa)$ and space-to-chord ratio (S/C) for high solidity (C/S) cases.

However, for cases with low solidity (e.g. propellers), this additional factor is not justified, and we found in the present study that a form without the additional $1/|n_\theta|$ factor gives better predictions. In the future, we will implement a formulation that blends the two different forms based on solidity, to yield a $|n_\theta|$ in the

denominator with low solidity, and revert to $|n_\theta|^2$ (as in [5, 6]) for high solidity.

Another model improvement introduced in this paper is the addition of a blockage term in the denominator of the inviscid and viscous forces, $\mathbf{f}_n$ and $\mathbf{f}_n$, to represent the reduction in blade pitch distance due to blade blockage, from $(2\pi\, r/B)$ to $(2\pi\, r/B)b$. In past work, we had only added the blockage factor b to the governing equations but not to the body force.

Lastly, Prandtl's tip load correction, defined in Equations (6) and (7), was applied to both inviscid and viscous body-forces to adapt the model from internal flow applications to external flow applications. It was found that this addition reduces thrust by around 3% and helps ease convergence difficulties caused by tip discontinuity.

Viscous Loss Generation. The viscous body-force, $\mathbf{f}_v$, is a dissipative force responsible for entropy generation simulating various loss mechanisms. The force is in the opposite direction to that of the blade relative flow and its magnitude is determined via

$$\mathbf{f}_v \;\equiv\; \frac{K_v\,(\frac{1}{2}\mathbf{W}^2)}{(2\pi r/B)\;b\;|n_\theta|}\,\hat{\mathbf{e}}_v\;. \tag{12}$$

where

$$\hat{\mathbf{e}}_v \;=\; -\,\frac{\mathbf{W}}{||\mathbf{W}||}\;. \tag{13}$$

Here K_v is a dissipation factor through which various loss mechanisms can be incorporated. A formulation for 2D profile losses takes the form

$$K_v \;=\; K_{v_o} \;+\; K_c\,K_{v_1}(\delta - \delta_{\text{ref}})^2 \tag{14}$$

to account for on-design losses (first term) and off-design losses (second term). The on-design losses are due to dissipation in boundary layers on both sides of the fictitious propeller blades for which we simply use flat plate solutions, and the on-design loss term is expressed as

$$K_{v_o} \;=\; 4.0\,C_{\mathcal{D}} \;+\; 3.0\,C_{\mathcal{D}}\,(K_c\,\pi\,\delta)^2\;, \tag{15}$$

with

$$C_{\mathcal{D}} = f(Re_\theta)\;. \tag{16}$$

The second term in Equation (15) reflects the local loading effect through differences between pressure and suction sides of the blade. The dissipation coefficient $C_{\mathcal{D}}$ is a function of the Reynolds number based on boundary layer momentum thickness, Re_θ, following the formulation in [12]. We used classical Blasius and turbulent 1/7 power boundary layer expressions to approximate θ locally. An example of Re_x, θ, Re_θ, and $C_{\mathcal{D}}$ distributions in the model region will be shown in the isolated propeller result section.

The second term in Equation (14), also referred to as the off-design term, provides a mechanism to simulate second order loss bucket effects and produces off-design behavior relative to a reference deviation angle distribution δ_{ref} as detailed in [5, 6]. Due to the relatively low blade loading in the propeller test case, off-design behavior only matters far from design operating conditions at very small advance ratios. Thus, the off-design term is turned off for the present study, and we simply set $K_v = K_{v_0}$.

Blade Metal Blockage. The effective reduction in mass flow due to blockage by blades with finite thickness is accounted for by incorporating a blockage factor

$$b \;=\; 1 \;-\; \frac{t}{(2\pi\, r/B)\,\cos(\kappa)}\;, \tag{17}$$

where t is the local thickness perpendicular to the camberline of the blade sections, and κ is the blade section stagger angle. This factor is unity in the absence of blockage and is added to the body-force and governing equations.

Blade metal blockage effects become important only when the number of blades is large or when the blade thickness is substantial, neither of which is the case for propellers. The meridional distribution of blockage

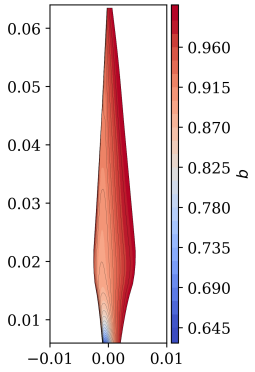

Figure 4: Blockage factor meridional contour for a propeller blade.

factor of the propeller used in this work, shown in Figure 4, indicates that the majority of the span has a blockage factor of over 90% except a very small area near the root. It is thus expected that the blockage has very small influence on the body-force prediction for propeller cases. On the other hand, the blockage will be more significant for high-solidity cases.

Governing Equations. The body force vector, $\mathbf{f}_{\mathrm{BF}} = \mathbf{f}_n + \mathbf{f}_v$, is included via source terms in the momentum and energy equations, and the compressible flow governing equations written as

$$\frac{\partial \rho}{\partial t} + \nabla \cdot (\rho \mathbf{V}) = -\frac{1}{b}(\rho\, \mathbf{V} \cdot \nabla b) \ , \tag{18}$$

$$\frac{\partial}{\partial t}(\rho \mathbf{V}) + \nabla \cdot (\rho\, \mathbf{V}\, \mathbf{V} + p\, \bar{\bar{I}} - \bar{\bar{\tau}}) = \rho\, \mathbf{f}_{\mathrm{BF}} + \frac{1}{b}(\bar{\bar{\tau}} - \rho\, \mathbf{V}\, \mathbf{V}) \cdot \nabla b \ , \tag{19}$$

$$\frac{\partial}{\partial t}(\rho\, e_t) + \nabla \cdot (\rho\, \mathbf{V}\, h_t - \bar{\bar{\tau}} \cdot \mathbf{V}) = \rho\, \mathbf{f}_{\mathrm{BF}} \cdot \mathbf{U} + \frac{1}{b}(\bar{\bar{\tau}} \cdot \mathbf{V} - \rho\, \mathbf{V}\, h_t) \cdot \nabla b \ . \tag{20}$$

Here ρ, p, $\mathbf{V}$, e_t, and h_t are the flow density, pressure, velocity, specific total energy, and specific total enthalpy, respectively, while $\bar{\bar{\tau}}$ is the shear stress tensor and $\bar{\bar{I}}$ the identity tensor. The vector $\mathbf{U} = \mathbf{\Omega} \times \mathbf{r}$ is the local blade velocity, set by the wheel speed and radial location. The additional terms with the blockage factor b represent the metal blockage effects as was derived in [6].

2.2 Blown-Lift Wing Geometry

As a test bed for studying the propulsor models' capabilities, we consider a blown-lift wing adopted from a sub-scale wind tunnel experiment conducted at MIT [13]. This wing features distributed propellers that produce a jet system blowing over the flapped wing for lift augmentation. In turn, the high-lift wing creates significant upstream influences that affects propeller performance. This interaction is a major characteristic of blown-lift designs.

The wing's geometrical specifications are listed in Table 1 and its 2D sectional geometry with propeller location shown in Figure 5. The original wing tested in the MIT wind tunnel has four propellers distributed evenly along the span and has walls on both ends of the span (end walls), thus represents a quasi-2D configuration with a 2D (infinite span) wing performance but fully 3D jet development.

For the sake of reducing computational cost, we only simulate a quarter of the span blown by a single propeller as shown on the right of Figure 5, with periodic boundary condition applied on the span-wise domain boundary faces to represent an infinite span. Only a small number of full-width four-propeller cases were conducted for the purpose of investigating jet mixing effects.

The propeller camber surface geometry and thickness distribution needed for the body-force model were extracted from the APC5x4E-4 propeller that the MIT wind tunnel experiments used [13]. This propeller has 4 blades with a diameter of 5 inches (0.127 m), and was tested experimentally at a maximum of 29000 RPM and produced up to 10.84 N of thrust.

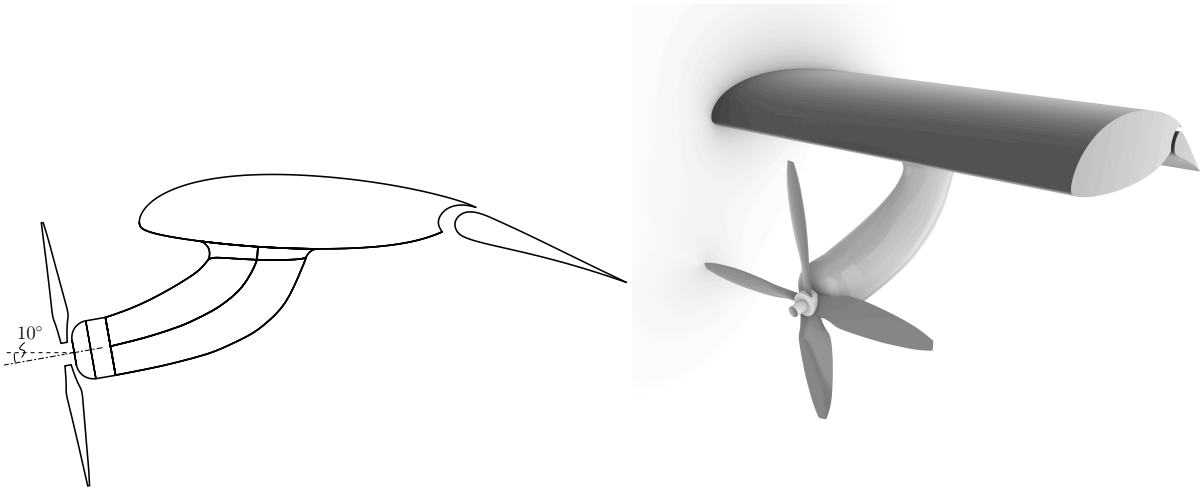

Figure 5: Blown-wing geometry used in wind tunnel tests by [13]: 2D airfoil geometry wth flap angle $\delta_f = 20°$ (left); and 3D geometry of quarter wing span with motor pylon and propeller (right).

Table 1: Geometrical parameters of the blown-lift wing.

Chord (at $\delta_f = 0°$)	0.2286 m
Span (per propeller)	0.1524 m
Motor axis angle	10°
Propeller tip diameter	0.127 m
Propeller hub diameter	0.0108 m
Propeller reference area	0.0126 m^2

2.3 Performance Metrics

The propeller operating point is set by the advance ratio

$$\lambda \equiv \frac{V_\infty}{\Omega R} \tag{21}$$

given a freestream velocity V_∞ and wheel speed Ω. Thrust coefficient is a measure of propeller performance and is defined as

$$c_{_T} \equiv \frac{T}{\frac{1}{2}\rho(\Omega R)^2 A_{\text{ref}}} , \tag{22}$$

where T is the propeller thrust, Ω the rotational speed of the propeller, and A_{ref} the propeller swept area as listed in Table 1. The power coefficient is defined from the shaft power P as

$$c_{_P} \equiv \frac{P}{\frac{1}{2}\rho(\Omega R)^3 A_{\text{ref}}} . \tag{23}$$

For the actuator disk model T is fixed as it is a model input. For the body-force model, we compute thrust and shaft power by integrating the source field region as

$$T_{\text{BF}} = \iiint_{\mathcal{V}} b\,\rho\,||\mathbf{f}_{\text{BF}}||_{_x}\,\mathrm{d}\mathcal{V} , \tag{24}$$

and

$$P_{\text{BF}} = \iiint_{\mathcal{V}} b\,\rho\,\mathbf{f}_{\text{BF}} \cdot \mathbf{U}\,\mathrm{d}\mathcal{V} = \Omega \iiint_{\mathcal{V}} b\,\rho\,||\mathbf{f}_{\text{BF}}||_{_\theta}\,r\,\mathrm{d}\mathcal{V} . \tag{25}$$

Entropy generation as a measure of losses is defined via Gibbs equation as

$$s - s_\infty = \frac{\mathcal{R}}{\gamma - 1} \ln\left(\frac{T}{T_\infty}\right) + \mathcal{R} \ln\left(\frac{\rho_\infty}{\rho}\right) \ . \tag{26}$$

where the reference state is taken to be set by freestream temperature and density, $\mathcal{R} = 287\,\mathrm{J/kg{\cdot}K}$ is the gas constant for standard air, and $\gamma = 1.4$ the air specific heat ratio. Note that in this equation only T denotes a temperature.

Aerodynamic efficiency of the propeller was defined as

$$\eta \ \equiv \ 1 - \frac{P_{\text{loss}}}{P_{\text{tot}}} \tag{27}$$

via the ratio of non-loss-generating power to total power produced by the propulsor model. Note that efficiency is only computed for the body-force model since its loss-generating force and non-loss-generating force are defined separately.

Pressure and total pressure are non-dimensionalized as pressure coefficient

$$C_p \ \equiv \ \frac{p - p_\infty}{\frac{1}{2}\rho V_\infty^2} \ , \tag{28}$$

and total pressure coefficient

$$C_{p_t} \ \equiv \ \frac{p_t - p_{t\infty}}{\frac{1}{2}\rho V_\infty^2} \ , \tag{29}$$

respectively.

2.4 Computational Approach and Setup

The open-source CFD code ADflow, a multi-block structured and overset finite volume solver developed at the University of Michigan [14], is used to carry out compressible Reynolds-Averaged Navier-Stokes (RANS) simulations with the Spalart-Allmaras turbulence model. The code uses second-order central difference discretization with matrix artificial dissipation. We use the fully implicit approximate Newton-Krylov (ANK) method [15] which relies on backward Euler's method to iteratively solve the system of equations. This allows the use of very large CFL numbers, an efficient startup for overset meshes, and thus faster convergence.

Both the actuator disk model and the body-force model are implemented in ADflow. To provide geometry input for the body-force model, the camber surface normals and thickness distribution are extracted from the actual propeller blade geometry and stored as volume structured-grid data. At the beginning of a simulation, this source structured grid is used by a geometric searching and interpolation algorithm within ADflow to transfer information from the source grid to the computational grid cells to which the body-force model should be applied. At runtime, a source term module within ADflow computes the body-force distribution based on the local flow conditions, blade geometry, and rotational blade speed. More details on the implementation of the body-force model can be found in [5].

All meshes are constructed using the commercial meshing software Pointwise. For blown-lift wing test cases, we took advantage of the ADflow's overset grid capability to mesh around the complex geometry of the flapped wing and motor pylon, and added a dedicated region for the propulsor model. Mesh convergence studies were performed separately for the wing mesh and the propulsor model region. These were carried out with 2D simulations of the wing airfoils due to the 2D nature of the wing meshes. Three mesh levels were created, and the coarsest of the three was chosen for the present study since it produces a less than 2% difference in force coefficients when compared with the finest mesh level.

For mesh in the body-force model region, due to the reliance on the actual blade geometry, grid finesse may influence the model's prediction of propeller performance. There needs to be enough cells in both the radial and axial directions to properly resolve the load distribution. Grid points are clustered near the leading and trailing edges of the model region where flow undergoes more rapid changes. The detailed model region mesh convergence is shown in the Appendix for the isolate propulsor study. The thickness of the actuator disk region was chosen such that it is similar to the average thickness of the body-force model region.

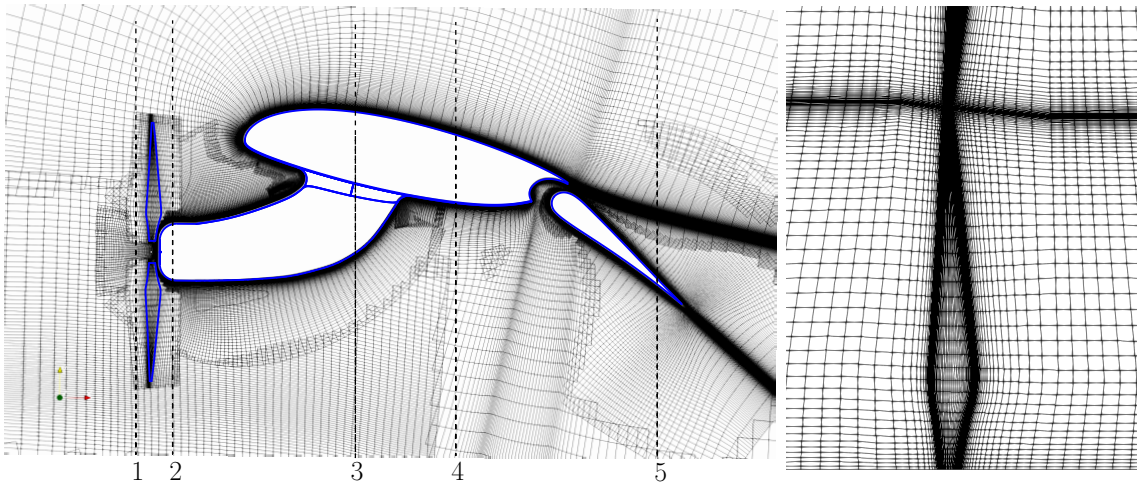

Figure 6: Spanwise cut view through the center of the propeller of the overset computational grids for the blown flapped wing at $\alpha = 10°$ (left), and meridional cut of the isolated propeller grid with the propeller hub at the bottom figure edge (right).

A side view of the assembled blown-lift wing computational grid close to the wing surfaces is shown in Figure 6. Axial measuring locations are labeled and marked with vertical dashed lines for reference in later sections. After the overset cutting, the mesh has a total of approximately 5.6 million compute cells with a y^+ of about unity on solid walls. The far-field domain boundaries extend more than 100 chords away from the wing surface in all directions.

Each single-propeller blown-wing solution was computed in around 600 to 800 CPU-hours with 32 processes on supercomputers at the Center for Advanced Research Computing (CARC) of the University of Southern California. Convergence reduction of 8 orders in total residual were generally achieved. Except for cases with more inherent unsteadiness, convergence may stall earlier, in which case care was taken to make sure that the lift and drag coefficients had converged. The computational cost of the body-force model is slightly higher than that to the actuator disk model due to its requirement of finer model region grids and some additional computations, but in practice the authors found the cost of solving with both models comparable due to the much higher cost of solving the rest of the problem.

Note that for the blown-wing cases, the propeller source region does not go beyond the hub of the propeller where the blade ends. In other words, the source region only covers the volume swept by the blades, and not the center hub and motor-mounting areas.

3 Isolated Propeller Results

In this section, the two propulsor models are applied to represent a stand-alone APC5x4-4 propeller with an uniform inflow that is aligned with its axis, implying that all solutions are axisymmetrical. We examine the local flow property for a nominal operating point, as specified in Table 2. The overall performance predicted by the body-force model is also shown for a range of operating points and compared with wind tunnel measurements.

Table 2: Operating condition of the examined isolated propeller case.

λ	0.085
V_∞	13.0 m/s
Ω	23 000 RPM
c_T	0.035

3.1 Local Flow Property Distributions

Figure 7 shows meridional contour plots of various flow properties within the body-force region that is marked by thin black lines. Pressure and total pressure rises are gradually produced across the propeller region, exhibiting unique gradient patterns linked to the blade geometry. A jet is produced as shown by the velocity contour, and swirl flow is generated with higher swirl angles near the root. Entropy is produced by the loss modeling within the body-force model. Higher loss is observed near the tip due to the higher blade-relative velocity and higher loading.

It can be seen that approximately 10% of the span near the hub has less effectiveness compare to the rest of span due to the lower blade tangential velocity and smaller chord. This part of the span produces much smaller pressure rise and work input, and blocks the flow by reducing axial velocity and producing a counter-swirl. However, the impact on performance is negligible and that hub region will be blocked by the motor once installed.

The distribution of various quantities computed by the body-force model are shown in Figure 8. They are related to fictitious blade relative flow and are used in the model formulation. These contours thus show the actual distributions used in the model description equations of Section 2.1.2.

Figure 9 shows the same set of flow contours produced by using the actuator disk model at the same condition. Overall, similar changes of flow properties across the blade region were observed when compared to that produced by the body-force model in Figure 7. The tip region flow properties reveal a smoother transition (smaller gradients) from the model region to the surrounding flow than that produced by the body-force model, since the latter's thickness reduces near the tip and thus causes sharper changes. Major

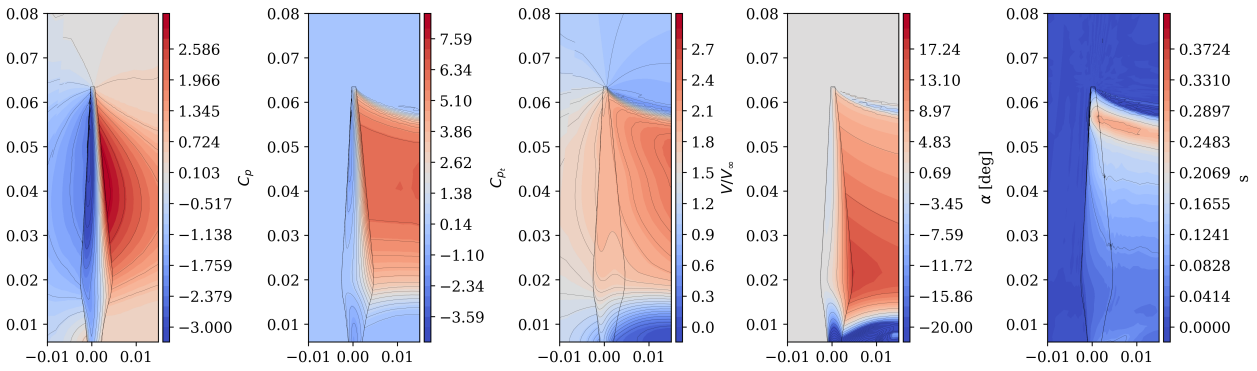

Figure 7: Flow contours predicted by the body-force model for isolated propulsor at $\lambda = 0.085$, $\Omega = 23000$ RPM: pressure coefficient, total pressure coefficient, normalized velocity, swirl angle, and entropy.

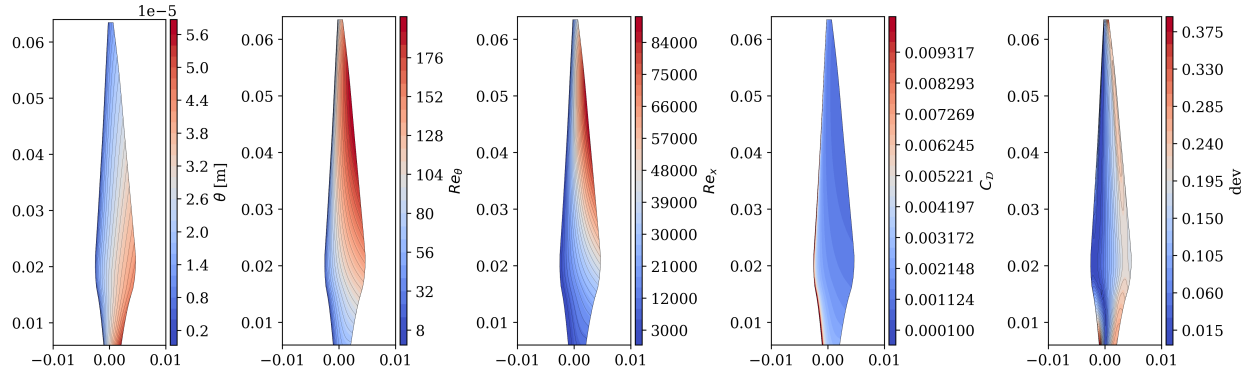

Figure 8: Contour of body-force model quantities for isolated propulsor at $\lambda = 0.085$, $\Omega = 23000\,RPM$: local momentum boundary layer thickness θ, Reynolds numbers Re_θ and Re_x, dissipation coefficient $C_\mathcal{D}$, and flow deviation angle δ.

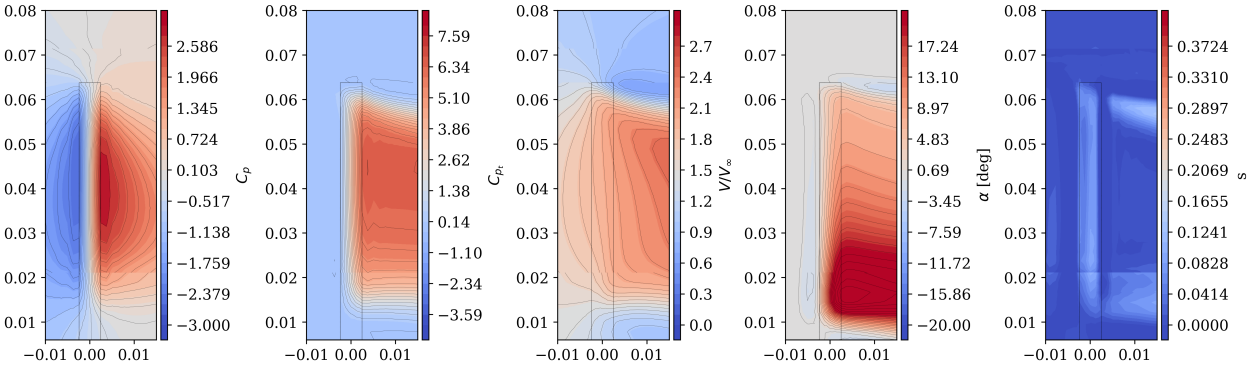

Figure 9: Flow contours predicted by the actuator disk model for isolated propulsor at $\lambda = 0.085$, $\Omega = 23000$ RPM: pressure coefficient, total pressure coefficient, normalized velocity, swirl angle, and entropy.

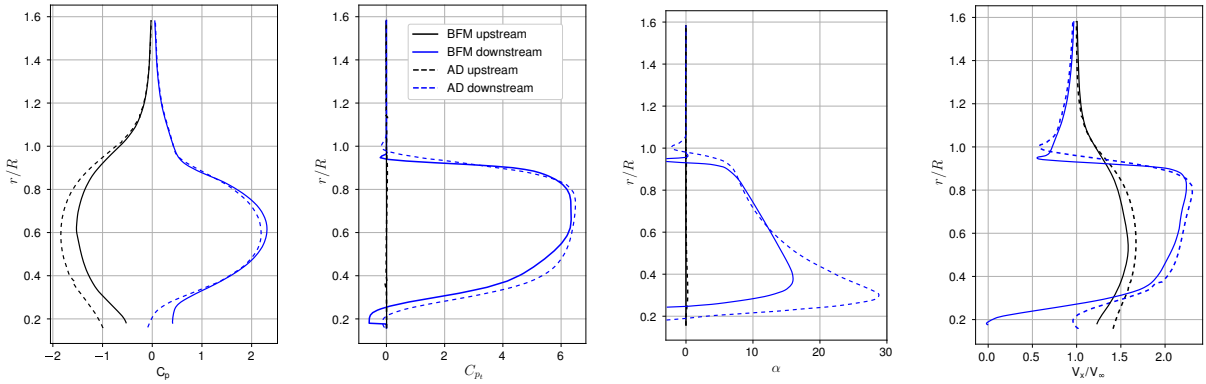

Figure 10: Radial profiles at upstream (station 1) and downstream (station 2) locations for isolated propulsor at $\lambda = 0.085$, $\Omega = 23000$ RPM: pressure coefficient, total pressure coefficient, swirl angle, and axial velocity.

differences between the models are found in entropy production, with the actuator disk producing an effect that is deemed non-physical and due to numerical errors. One of the shortcomings of the actuator disk model is that it does not include a mechanism to represent loss generation.

Quantitative comparison of the radial profiles of several flow properties taken at locations upstream (station 1) and downstream (station 2) of the propulsor model region are shown in Figure 10. Despite fundamental differences in the two modeling approaches (one using the blade geometry and the other a prescribed load distribution), the predicted radial profiles agrees very well for C_p, C_{p_t}, and axial velocity for this isolated propeller case. This is likely because this particular propeller (and its geometry used by the body-force) does produce a close-to-optimal loading (which is well-described by the distribution imposed in the actuator disk model). On the other hand, large differences are seen in the absolute swirl angle away from the tip, with the actuator disk model creating nearly twice as much flow swirl at 30% of the span. This is likely due to the simple estimations of circumferential force as scaling with $1/r$, which thus becoming inaccurate at very small radii.

3.2 Overall Performance Predicted by Body-Force Model

Figure 11 shows the characteristic of the isolated APC5x4-4 propeller over a range of operating points as predicted by the body-force model with comparisons to wind tunnel measurements [13] and Qprop prediction. The body-force model predicts the experimental propeller $c_T - \lambda$ characteristic slope well, and is slightly off in magnitude with an approximately 5% over-prediction over most of the operating range when compared with the wind tunnel measurements. The body-force prediction also closely matches results from Qprop[1], even though the latter could be expected to over-predict the performance of small propellers with low Reynolds numbers like this one. The operating point where thrust reduces to zero (around $\lambda = 0.2$) is well predicted by the body-force model. Performance predictions with the body-force model at small advance ratios (λ<0.03) could be improved by adding the off-design term, which was not applied in this work due to its lower importance in this application.

With the advantage of profile loss modeling, the body-force model predicts the physically correct trend in propeller aerodynamic efficiency. Its predictions show lower efficiency at higher advance ratio until the thrust reduces to zero. We would see the efficiency drop at very low advance ratios if the off-design loss model was included. Physically correct variations of power coefficient was also observed, with a higher required shaft power at lower advance ratio.

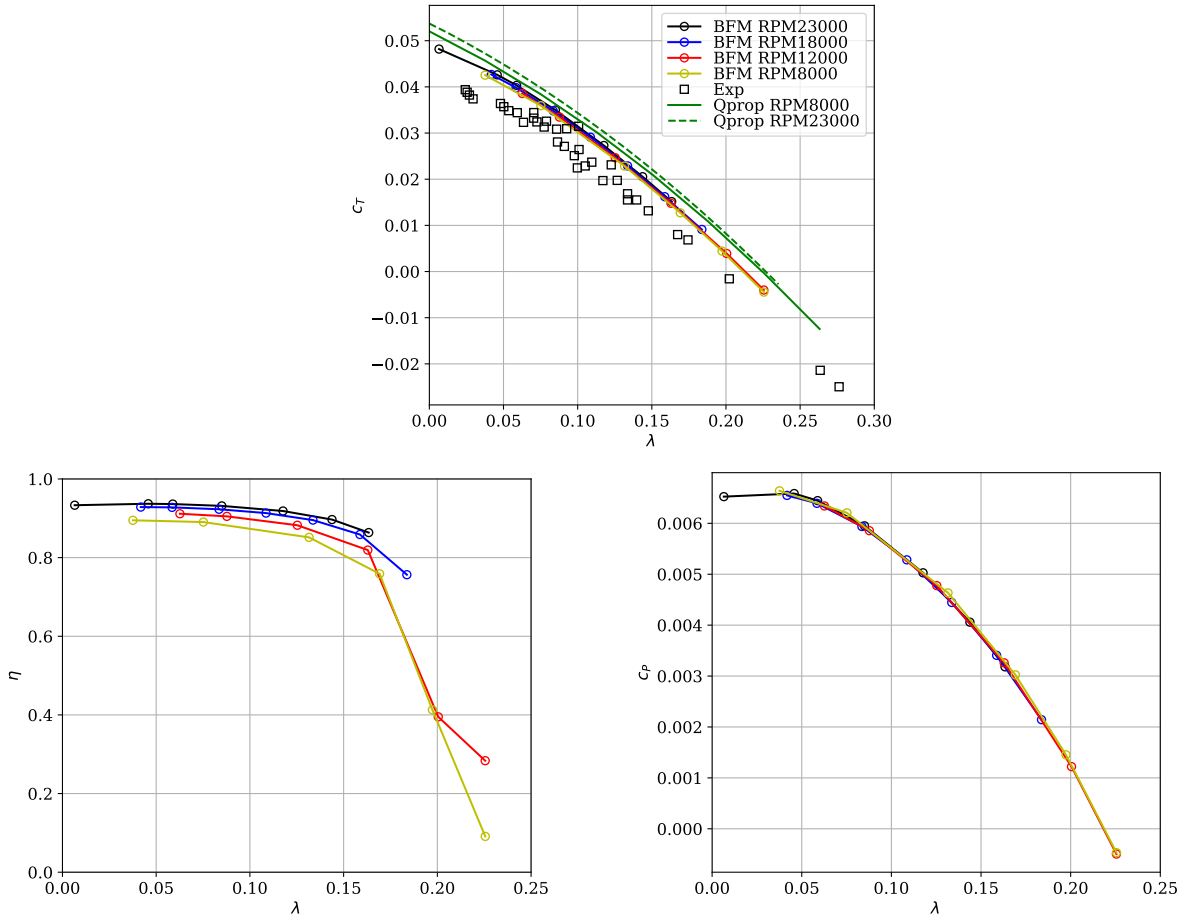

Figure 11: Overall propeller performance for isolated propeller: thrust coefficient (top), aerodynamic efficiency (bottom left), and power coefficient (bottom right) versus advance ratio λ. Comparison between body-force model (BFM), and both wind tunnel measurements (Exp) from [13] and Qprop predictions.

[1] a classical blade-element/vortex code developed by Mark Drela at MIT

4 Wing-Propeller Interactions

In this section, we consider the blown-wing test case and focus on understanding how the interactions between wing and propeller affects each other's performance, and on how well this interaction is captured by each of the propulsor models.

The flow fields at a reference operating condition, defined in Table 3, is used to describe the basic features found in blown-lift wings flowfields and understand the model response to propeller inflow. This chosen operating point represents a high-lift condition representative of what is desirable for ultra short-distance take-off or landing. We then analyze the aero-propulsive performance and the interaction between wing and propeller, before looking more closely at the propeller jet development and mixing.

Table 3: Reference operating conditions for the blown-lift case. The body-force model operating condition is set via the wheel speed Ω, and the actuator disk model condition is set via the isolated thrust magnitude.

α	8°
δ_f	30.0°
V_∞	12.7 m/s
λ	0.08
Ω	23 900 RPM
c_T (isolated)	0.036

4.1 Basic Features of the Flow Over a Blown-Wing

Figure 12 shows velocity contour on a wing cross-section through the propeller center, as predicted by the body-force model and the actuator disk model at the reference condition. The basic flow features of a blown-lift wing are evident in this view. A jet produced by the propeller blows over the wing and energizes the flap boundary layers through the slot. This allows the flow over the flap to remain attached even at high angle

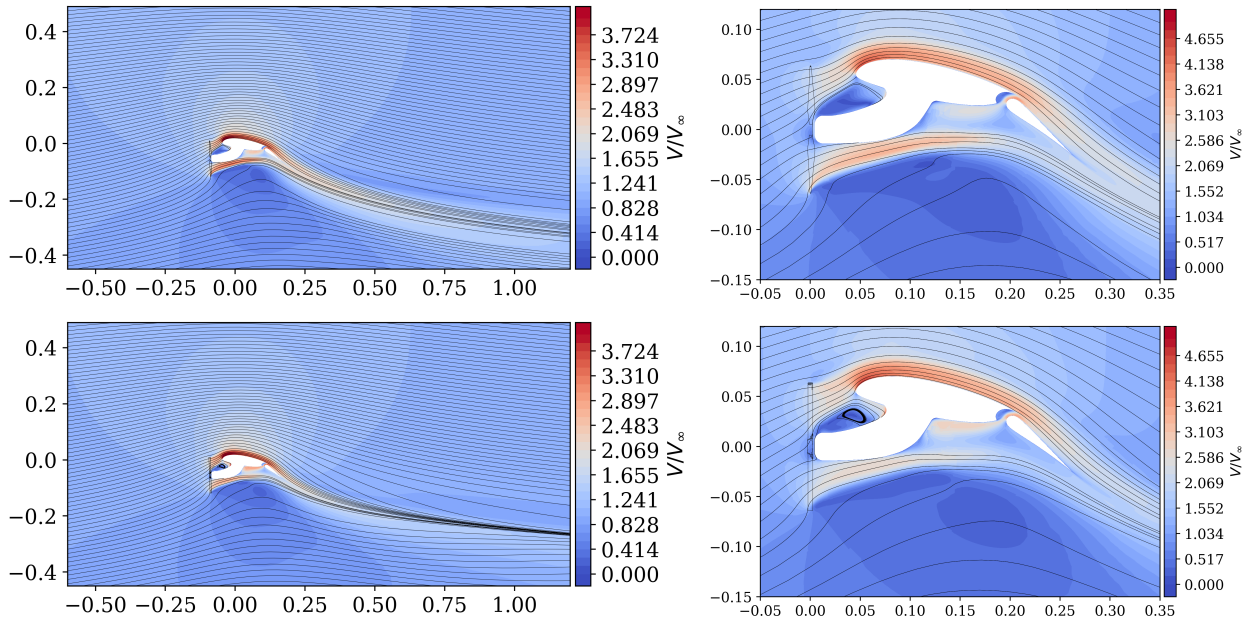

Figure 12: Velocity contours of wing sectional flow at the reference condition with the body-force model (top) and the actuator disk model (bottom), in a zoomed-out view (left) and zoomed-in view (right).

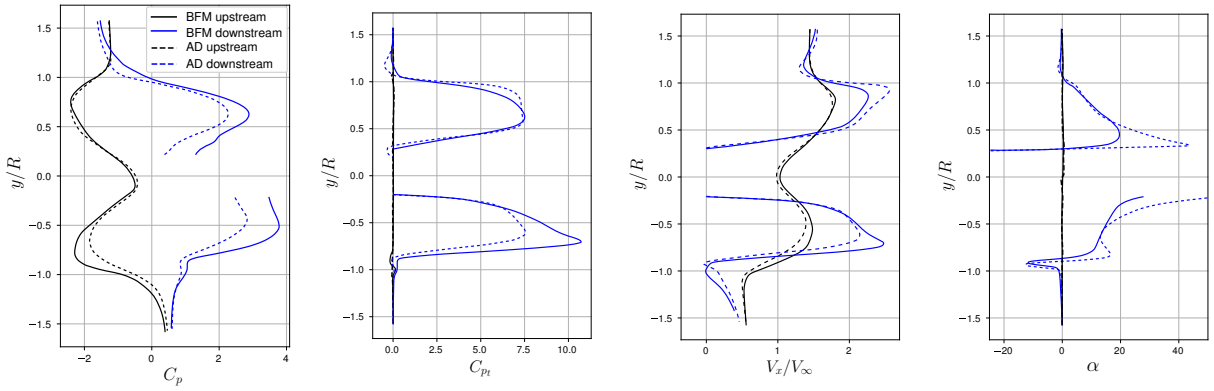

Figure 13: Vertical profiles for blow-lift case reference condition at upstream (station 1) and downstream (station 2) locations: pressure coefficient, total pressure coefficient, normalized axial velocity, and swirl angle.

of attack and with high flap deflection angles, thus generating high lift. The jet is also deflected downwards by the flapped, which also provides lift. A consequence of the high lift and corresponding high circulation is that the bending of the streamlines and their very large curvature causes the propeller to operate with its axis misaligned with the inflow, as can be seen from the streamlines in the figure.

Some differences between the results from the two models can be observed. The velocity magnitude contours indicated that the body-force model produces stronger blowing at the bottom of the propeller than the actuator disk model and, as result, more flow deflection is produced far downstream of the wing as indicated by the streamline directions (left side of Figure 12). This contributes to predicting a higher lift and pitching moment from the blown-wing as will be shown in the wing performance results of Section 4.3.

The sampled flow properties, or profiles, along vertical lines upstream (station 1) and downstream (station 2) of the propulsor model region are shown in Figure 13. These are taken along a line through propulsor center that is perpendicular to the propeller axis as illustrated in Figure 6. These profiles confirm that overall the body-force model predicts higher static and total pressure rises than the actuator disk model. Furthermore, whereas the actuator disk model produces relatively similar changes at the top and bottom of the propeller, the body-force results in higher pressure (total and static) rises and higher jet velocity being generated at the propeller's bottom than at its top. This results in a nearly 15% higher maximum C_p rise and a 42% higher maximum C_{p_t} rise at the propeller bottom than at its top in the simulations with the body-force model.

On the axial velocity profile, we can see that the upstream location has higher V_x at the top of the propeller than at the bottom, irrespective of which model is used. The models however differ in downstream axial velocity prediction: the body-force model rises the velocity more at the bottom enough to invert the top-bottom ratio of the upstream station, and thus results in a higher axial velocity at the bottom than at the top. The actuator disk model, on the other hand, maintains similar relative magnitudes between top and bottom at the downstream station (i.e. higher at the top). Finally, both models produce similar amounts of overall swirl, but the actuator disk induces higher swirl levels near the hub.

The above results clearly show that the propulsor models react differently to the misaligned inflow, while they behaved similarly for the isolated propulsor. Since propeller jets are crucial components of the blown-lift system which impact the overall performance by affecting the forces experienced by the wing, the observed differences emphasize the importance of choosing the correct propeller models for such applications. In order to better explain the observed differences, we will examine the non-uniform propeller flow on axial planes in the next section.

4.2 Propeller Inflow Non-Uniformity and Model Response

The high lift from the blown-wing produces a significant upstream influence that changes the propeller's operating condition. Figure 14 shows the flow contours on axial planes for various flow properties overlaid with arrows that indicate flow velocity directions measured upstream (station 1) and downstream (station 2) of the propeller. Axial planes in this paper are perpendicular to the propeller axis and the contours plotted looking downstream. Also note that the rotation direction of the propeller is clockwise in this view.

Propeller inflow non-uniformity is primarily characterized by two mechanisms, both of which are the result of large upstream flow curvatures that causes the propulsor's inflow to be at large and non-uniform incidence angles. First, the propeller inflow shows lower axial velocity at the bottom due to locally higher inflow misalignment, as seen in Figure 14(a) and as indicated by the direction of the streamlines in Figure 12. Higher axial velocity at the top is also contributed by the suction (and hence higher acceleration) on the wing leading edge. This non-uniform axial velocity distribution implies that the propeller is operating with locally smaller advance ratio at the bottom than at the top, thus with higher loading at the bottom. The body-force model produced the expected response as shown by the downstream C_{p_t} contours of Figure 14(d), which confirm the higher work input from the propeller bottom.

The second effect is swirl flow non-uniformity caused by the overall up-wash experienced at the propeller location. This can be better seen in the upstream swirl velocity contours of Figure 14(b), which indicate a co-swirl (red) region on the left and a counter-swirl (blue) region on the right. Thus, the up-wash compounds with the propeller rotation on the co-swirl (left) side and counter-acts it on the counter-swirl (right) side. In other words, the counter-swirl side of the propeller blade is operating with higher blade incidence angles and thus bears higher loading, and vise versa for the co-swirl side. The body-force model produced the expected

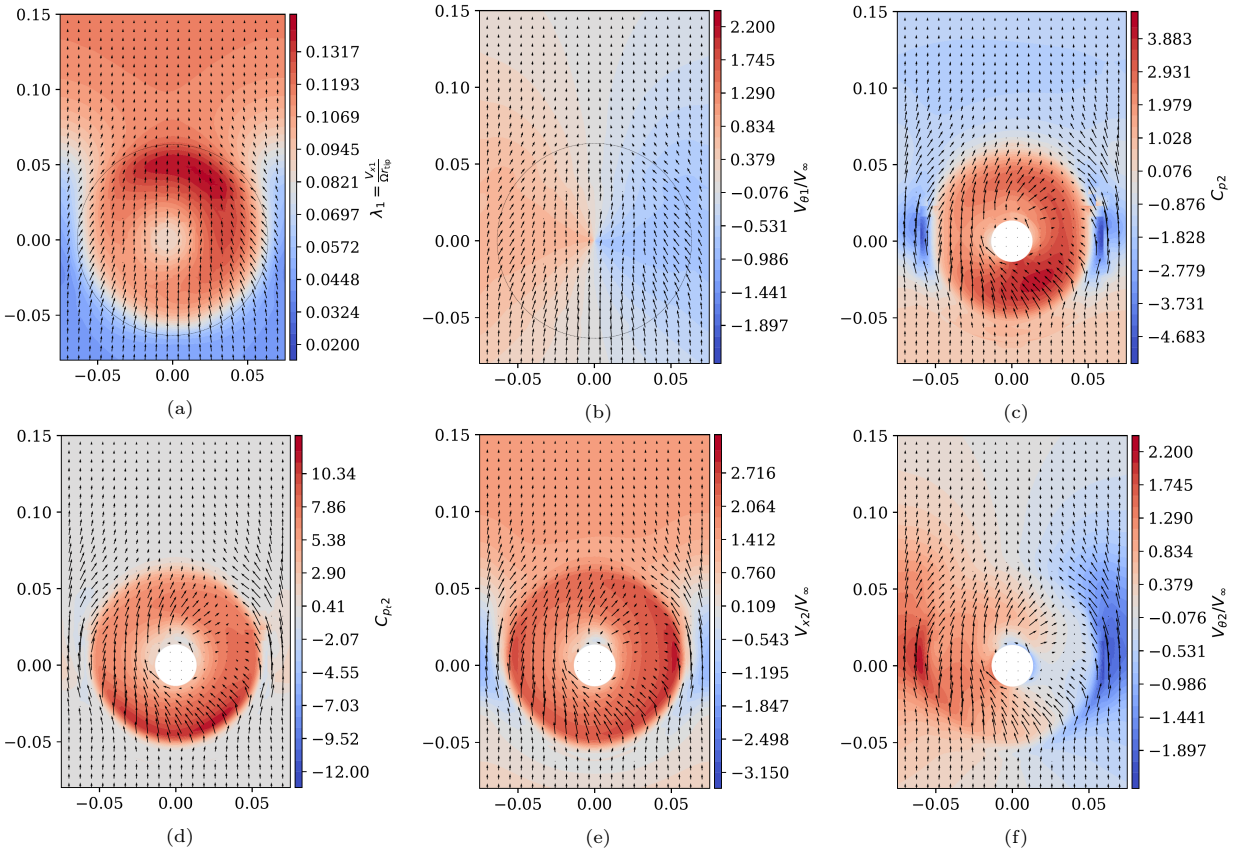

Figure 14: Body-force model solution: upstream (station 1) contours of local advance ratio (a), and normalized swirl velocity (b); and downstream (station 2) contours of pressure coefficient (c), total pressure coefficient (d), normalized axial velocity (e), and normalized swirl velocity (f).

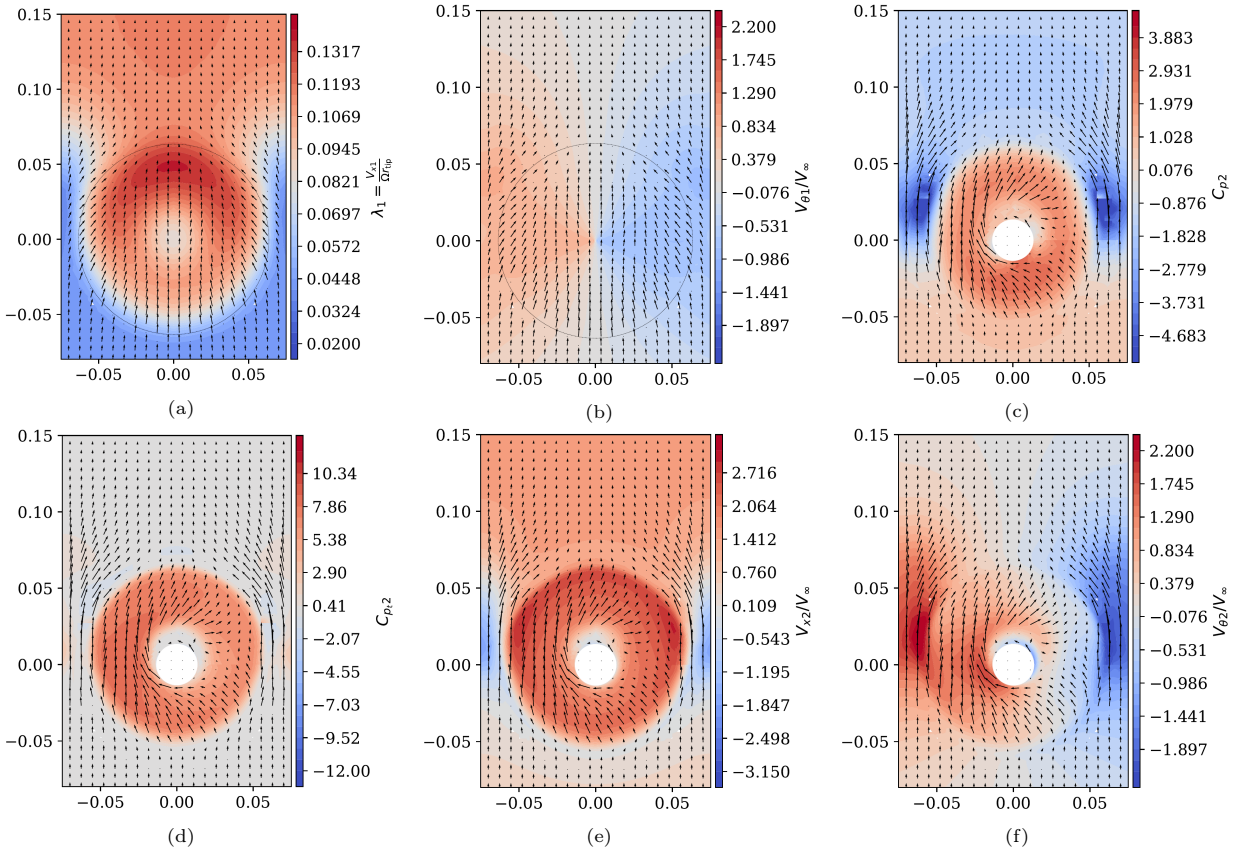

Figure 15: Actuator disk model solution: upstream (station 1) contours of local advance ratio (a), and normalized swirl velocity (b); and downstream (station 2) contours of pressure coefficient (c), total pressure coefficient (d), normalized axial velocity (e), and normalized swirl velocity (f).

response by creating slightly higher work input (as reveled in downstream C_{p_t}), higher axial velocity rise, and higher pressure rise on the right side of the propeller.

In addition to affecting the loading, the incoming swirl non-uniformity impacts the downstream swirl field. The resulted downstream (station 2) swirl velocity distribution of Figure 14(f) shows that significantly higher swirl velocity is produced by the co-swirl (left) side of the propeller than the counter-swirl (right) side, with on the right side the swirl produced by the propeller almost canceling out the upstream counter-swirl. This unbalanced swirl velocity distribution at the downstream location influences how the jet then propagates and mixes.

In terms of relative importance of these two effects (V_x versus V_θ non-uniformities), the downstream total pressure contours show stronger gradients (more work input) near the bottom than on the right, thus indicating that the impact from the inflow axial velocity non-uniformity (more pronounced at the bottom) is more significant than that from the swirl distribution non-uniformity (more important on the right).

The same set of axial flow contours as predicted by the actuator disk model are shown in Figure 15. Similar upstream non-uniform conditions can be seen from Figure 15(a) and (b) except that the advance ratio distribution appears to be more left-right symmetrical than it was for the body-force model, due to a more symmetrical axial velocity profile (streamtube contraction). The downstream C_{p_t} contour is relatively uniform with slightly higher work input from the left. As such, upstream non-uniformity in axial velocity and swirl distribution is not correctly reflected by the actuator disk work input, due to its prescribed and fixed loading. Downstream swirl distribution is more similar to that predicted by the body-force model due to a circumferentially uniform swirl flow added by the advanced actuator disk model we are using, except for the higher downstream flow swirl near the hub that was already observed in the isolated propeller case.

4.3 Coupled Wing and Propeller Performances

Propeller performance parameters including thrust coefficient, power coefficient and aerodynamic efficiency are plotted as a function of angle of attacks in Figure 16 for the two propulsor models. These performance variations illustrate the impact of inflow misalignment and non-uniformity produced by the wing's influence on the predicted propeller performance. Note that the thrust value shown in the figure for the actuator disk results is computed by integrating the source field (and match the specified thrust model value).

This blown-lift wing test case is an example of a highly coupled propulsor-airframe system. It is worth noting that although the propeller is aligned with the freestream flow direction (*i.e.* far upstream outside of wing's influence) when the wing is at an angle of attack of $\alpha = 10^\circ$ (due to the propeller being installed 10° pitching-down), the actual propeller inflow was observed to be aligned with the propeller axis at an α between -8° and -10° instead. Overall, there is thus a nearly 20° difference between the freestream direction and the propeller axis when the wing is at $\alpha = -10^\circ$, *i.e.*, a nearly 20° up-wash at the propeller location due to the very high lift generated by the wing. Thus, it is clear that the presence of the wing strongly influence (via the lift/up-wash) the propulsor flow. Conversely, the propulsor jet is responsible for some lift-augmentation effect on the wing flap, and therefore the propulsor flow in turn influences the wing and its lift.

At $\alpha = -10^\circ$ wing angle of attack, the propeller thrust coefficient when predicted by the body-force model is undistinguishable (within 0.8%) from that for the isolated propulsor, a reflection of the fact that the propeller inflow is aligned with the propeller axis at this condition and that the major wing influence on the propeller is exerted via flow direction changes more than non-uniformities. As the angle of attack increases, thrust output from the actuator disk model remains constant despite flowfield changes, whereas the body-force model produces increasing thrust levels. A 11% thrust increase is seen across the range of angle of attacks studied ($\alpha \in [-10^\circ, 15^\circ]$) as predicted by the body-force model. This is the effect of inflow misalignment and wing influence as previous explained. It was shown in a relevant study [16] that an isolated propeller produces higher thrust at a larger angle with respect to freestream: the presence of the high-lift wing exaggerates this effect. This increase of thrust output is not captured by the actuator disk model since its thrust value is prescribed as an input parameter.

Propeller power and aerodynamic efficiency were only computed for the body-force model. The power coefficient is seen to initially increase with angle of attacks due to higher required power to maintain the increasing loading. The competing factor of increasing average axial inflow velocity (thus advance ratio) takes effect at higher angles of attack where the power coefficient start to decrease. The maximum predicted shaft power occurs near $\alpha = 5^\circ$. The maximum propeller efficiency is found to be 89% (while it was 93% in the isolated propulsor case), and the efficiency curve has a relatively flat optimal region over α values between 0° and 5°, where the propeller experiences moderate misalignment and produces higher thrust.

Figure 17 shows the lift, drag and pitching moment coefficients of the blown-lift wing as function of angle of attack, to illustrate how the blown-wing performance gets influenced by the propulsor models. Note that these coefficients are computed (defined) by integrating the surface stresses on the wing-and-pylon only (*i.e.* the propeller force contribution was not included), and then projecting along the freestream and normal

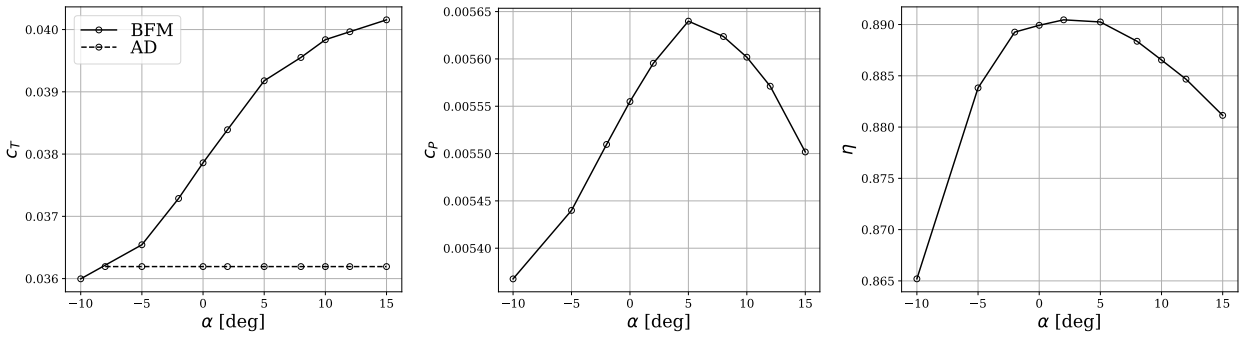

Figure 16: Propeller performance parameters as function of wing angle of attack: comparison between body-force model (BFM) and actuator disk (AD) model predictions.

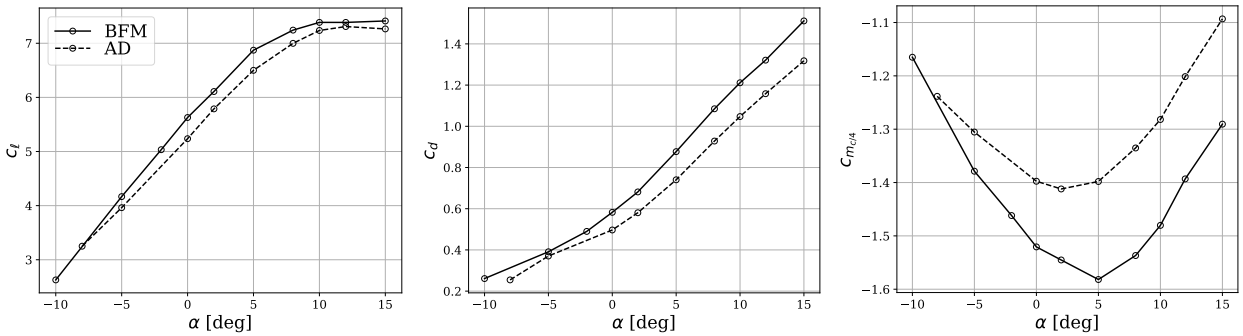

Figure 17: Wing force and moment coefficients as function of angle of attack: comparison between body-force model (BFM) and actuator disk (AD) model predictions.

directions. Similar trends are seen from the two models but discrepancies in magnitudes exist. By using the body-force model, the blown wing produced on average 5% larger c_ℓ, 18% larger c_d, and 18% larger c_m magnitude than what the actuator disk model predicts, with slightly higher slopes in lift and drag curves. Significant differences in pitching moment slopes are observed between $-10°$ and $5°$ angle of attack, with magnitude differences overall, and these prediction differences could potentially have an impact on aircraft control considerations. The difference between models diminishes as the angle of attack is reduced due to better alignment of the propeller plane with the local flow direction. The observed difference in forces and moments are the product of the different responses from each propulsor model at various angles of attack, and the result of slightly different jets blowing over the wing and being deflected by the flap. Therefore, the propulsor model's response to wing influence does make a large enough difference in wing performance (in addition to the difference already shown for propulsor performance) to justify the need for an advanced propulsor model that can adapt to non-uniform flow variations.

From the comparison between the models for the blown-lift simulations, it is evident that the body-force model is able to adapt to the inflow variation caused by wing influence and produces a physical response that better mimics real propeller operation, while the actuator disk model fails to capture the interactions and requires a set thrust level.

4.4 Jet Mixing

An important flow feature of the DEP blown-lift wing is the mixing of the propeller jets. Test cases with the full wing span and four propellers and zero angle of attack were created to visualize the jet mixing process.

Figure 18 shows contours of C_{p_t} on axial planes placed at the streamwise stations when looking downstream, with vertical lines indicating the propeller center spanwise positions. The closely spaced propellers produce jets that gradually mix and coalesce into a jet sheet with an irregular pattern that moves slightly to the left as it travels downstream. This irregular jet profile is shaped by two mechanisms: the unbalanced swirl distribution (as shown in Figure 14(f)) and the blockage by the motor pylon as revealed in Figure 19. The stronger swirl region seen on the propeller's left side is deflected towards the top left by the motor pylon and impinges onto the main wing element. This in turn generates a leftward motion at the bottom of the motor pylon near station 3, clearly visible in Figure 19, which pushes the jet from that propulsor into the neighboring jet. This pattern is very similar to the jet-wake pattern reported in the wind tunnel experiments [13]. The leftward jet motion could be much more pronounced in a 3D full aircraft situation where the wing tip is unbounded. If all propellers on a wing rotate in this clockwise direction (as seen from the front), then the leftward motion induced by the outer-most propeller would compound with the motion induced by the tip vortex (from lower surface to upper surface) near on the left wing tip, but oppose the tip vortex motion near the right wing tip.

Figure 18 also shows the jet mixing process produced by the actuator disk model. Comparing the prediction made by the two models, minor difference in jet patterns can be seen due to difference in swirl distributions and pressure rise, but overall a similar mixing process is observed. In addition, the body-force produced jets that appear to be more non-uniform probably due to its response to inflow non-uniformity.

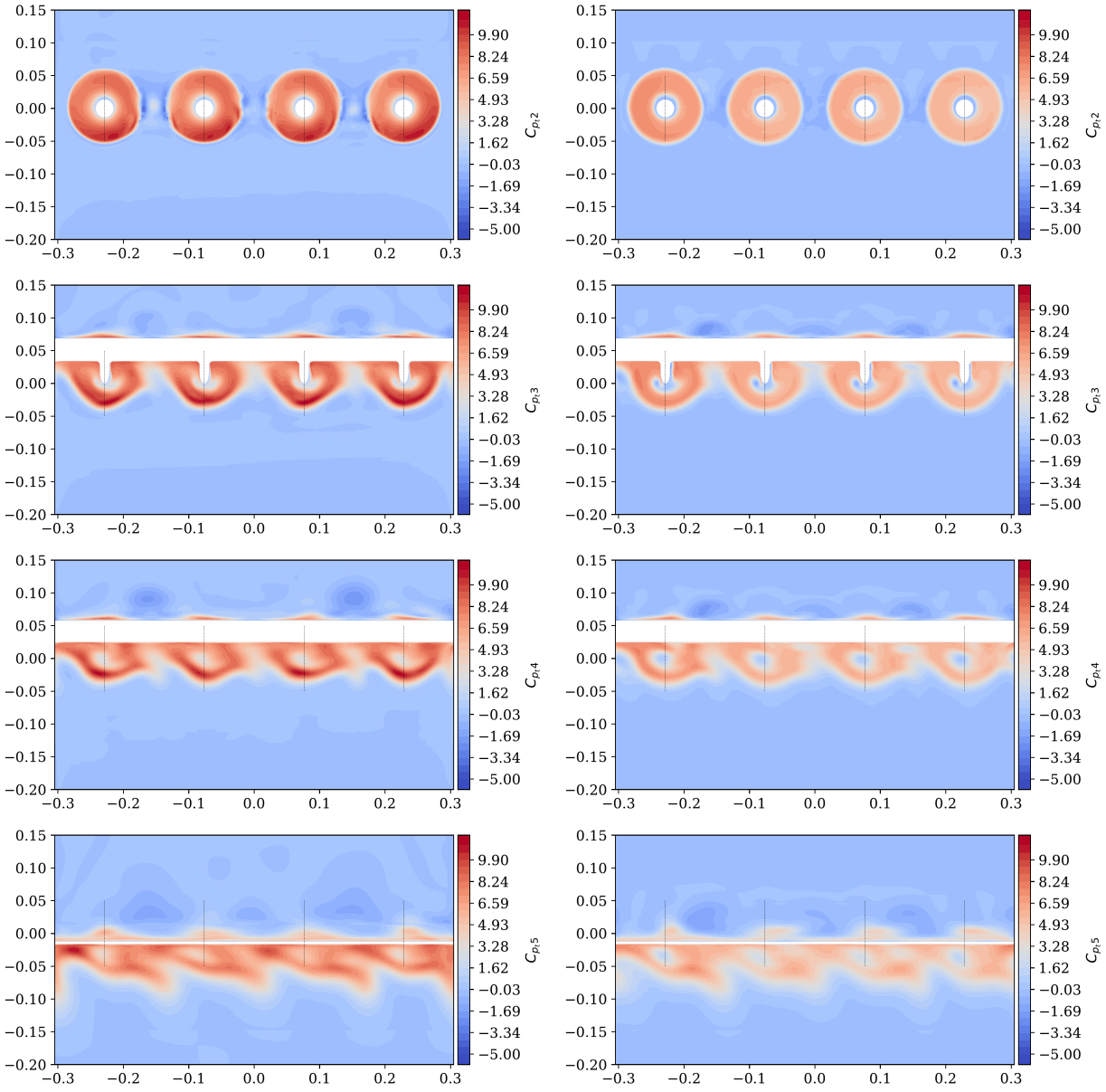

Figure 18: Jet mixing produced by the body-force model (left column) and by the actuator disk model (right column), as seen from total pressure contours on axial planes at different streamwise stations. Vertical lines mark the propeller location, and propeller rotation is clockwise.

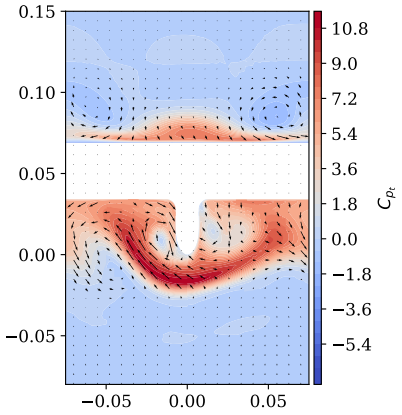

Figure 19: Total pressure contour on axial plane near the motor pylon at station 3: the swirl flow is blocked by the pylon, inducing a leftward motion at the bottom of the pylon.

5 Summary and Conclusions

A new body-force propulsor model has been implemented to represent propellers in high-fidelity CFD simulations of a blown-lift wing, a test case with strong propulsor-airframe interactions, and compared with results using an advanced actuator disk model and experimental data. The overall goal was to validate the body-force model for propeller applications, and investigate the extent to which the propulsor models are able to capture the complex aero-propulsive interactions between the wing and the propellers.

The body-force modeling approach relies on rotor blade geometry and rotational speed to generate a source field that mimics the effect of the blades on the flow, including work input and loss generation. By taking into account the local flow conditions, the model is able to produce a realistic response.

The body-force model's prediction capabilities was assessed first for an isolated propeller with a uniform inflow aligned with propeller axis. The results show that the body-force model predicts the propeller's $c_T - \lambda$ characteristic within 5% of experiment measurements and produces a realistic trend for efficiency and power variation. The actuator disk model uses the thrust value as an input, and produced similar flow fields as the body-force model including pressure rise, total pressure rise, and axial velocity. Radial sampling of the flow field showed overall similar pressure and velocity profiles, but higher swirl angle was observed near the hub from the actuator disk model due to its simple estimation of circumferential forces which becomes inaccurate at smaller radius.

The wing-propeller flow interaction was investigated via a blown-lift wing test cases. It was found that the propeller operates under inflow conditions with non-uniformities in both axial velocity (thus advance ratio) and swirl velocity, due to the large up-wash at propeller location that is produced by the high-lift wing. The body-force model predicts more realistic response by producing higher pressure (total and static) rise and higher jet velocity in areas with locally lower advance ratio and upstream counter-swirl. An unbalanced downstream swirl distribution was observed as result of upstream non-uniformities which impacts how the propeller jets develop and mix. Across a sweep over a range of angle of attacks, the body-force model produces higher thrust at higher angles of attack thanks to its ability to adjust to the varying inflow conditions caused by misalignment, while the actuator disk was unable to react as it maintains a constant thrust.

The blown-lift wing performance was also affected by the different propulsor model responses. On average, 5% higher lift, 18% higher drag and 18% higher pitching moment was observed when using the body-force model. Significant differences in pitching moment slopes and magnitudes are observed, an important consideration when selecting a model for estimating aircraft stability and control. More jet flow deflection by the flapped wing was observed from cases using the body-force model, an effect that partially contributes to the higher lift and pitching moment. Similar jet mixing processes were produced by both models, and the jet-wake pattern at flap trailing edge was found to be similar to that reported in wind tunnel experiments.

Overall, the body-force model was shown to be able to capture the wing-propeller interaction effects better than the actuator disk model. To be able to more accurately predict distributed electric propulsion

(DEP) and blown-wing performance with strong aero-propulsive coupling, an advanced propulsor model that is able to adapt to the varying local flow conditions is required, such as the body-force model presented in this work.

Acknowledgements

This research was funded in part by a NASA STTR Phase I program carried out in collaboration with Electra.aero (Contract Number 80NSSC21C0367, May 2021 – June 2022). The authors would also like to acknowledge the Center for Advanced Research Computing (CARC) at the University of Southern California for providing computing resources that have contributed to the research results reported within this publication (URL: https://carc.usc.edu).

References

[1] Jason Welstead and James L. Felder. Conceptual design of a single-aisle turboelectric commercial transport with fuselage boundary layer ingestion. In *AIAA 2016-1027, AIAA SciTech, 54nd Aerospace Sciences Meeting, 4–8 Jan 2016, San Diego, CA*, 2016.

[2] Alejandra Uranga, Mark Drela, Edward Greitzer, Neil Titchener, Michael Lieu, Nina Siu, Arthur Huang, Gregory M. Gatlin, and Judith Hannon. Preliminary experimental assessment of the boundary layer ingestion benefit for the d8 aircraft. In *AIAA SciTech, 52nd Aerospace Sciences Meeting, 13–17 Jan 2014, National Harbor, MD*, 2014.

[3] Mark Drela. Development of the D8 transport configuration. In *29th AIAA Applied Aerodynamics Conference*, page 3970, 2011.

[4] Alejandra Uranga, Mark Drela, David K. Hall, and Edward M. Greitzer. Analysis of the aerodynamic benefit from boundary layer ingestion for transport aircraft. *AIAA Journal*, 56(11):4271–4281, 2018.

[5] Tianbo Xie and Alejandra Uranga. Development and validation of non-axisymmetric body-force propulsor model. In *AIAA 2020-3578, AIAA Propulsion and Energy 2020 Forum*, 2020.

[6] Tianbo Xie and Alejandra Uranga. Capturing aero-propulsive coupling effects with a body-force propulsor model. In *AIAA Propulsion and Energy 2021 Forum*, page 3456, 2021.

[7] Frank E. Marble. *Three-Dimensional Flow in Turbomachines*, pages 83–166. Princeton University Press, 1964.

[8] Yifang Gong. *A Computational Model for Rotating Stall and Inlet Distortion in Multistage Compressors*. PhD thesis, Massachusetts Institute of Technology, 1999.

[9] D. K. Hall, E. M. Greiter, and C. S. Tan. Analysis of fan stage design attributes for boundary layer ingestion. *Journal of Turbomachinery*, 139(7):071012–1–10, July 2017.

[10] Cécile Casses, Christopher Courtin, Mark Drela, Thomas Fitzgibbon, Runda Ji, Maciej Skarysz, Spalart Philippe, and Qiqi Wang. Impact of the propulsion modeling approach on high-lift force predictions of propeller-blown wings. In *AIAA AVIATION 2022 FORUM*, 2022.

[11] F. S. Weinig. *Theory Of Two-Dimensional Flow Through Cascades*, pages 13–82. Princeton University Press, 1964.

[12] J. D. Denton. The 1993 IGTI Scholar Lecture: Loss Mechanisms in Turbomachines. *Journal of Turbomachinery*, 115(4):621, 1993.

[13] Trevor Long. An Experimental Investigation of Propeller Blown-Flap Airfoils. , Master Thesis, Massachusetts Institute of Technology, 2021.

[14] Charles A Mader, Gaetan KW Kenway, Anil Yildirim, and Joaquim RRA Martins. Adflow: An open-source computational fluid dynamics solver for aerodynamic and multidisciplinary optimization. *Journal of Aerospace Information Systems*, 17(9):508–527, 2020.

[15] Anil Yildirim, Gaetan K. W. Kenway, Charles A. Mader, and Joaquim R. R. A. Martins. A jacobian-free approximate newton– krylov startup strategy for rans simulations. *Journal of Computational Physics*, page 108741, November 2019.

[16] Racheal M Erhard and Juan J Alonso. A comparison of propeller wake models for distributed electric propulsion and evtol aircraft in complex flow conditions. In *AIAA SCITECH 2022 Forum*, page 1676, 2022.

Appendix: Grid Convergence

Three model grid levels, as shown in Table 4, were created and tested with the isolated propeller setup using the body-force model. The resulted thrust and shaft power are plotted in Figure 20. Less than 1% difference in the produced thrust and shaft power was seen across all grid levels. We chose the medium model grid level for the blown-lift wing case to better resolve flow non-uniformities. For the isolated propeller case, due to its lower computational cost, a finer 50x50x180 model region grid was used for a better visulization resolution.

Table 4: Grid refinement levels for mesh convergence study: number of cells across the body-force model region in chordwise direction (N_c), radial direction (N_r) and tangential direction (N_t), and total number of cells (N_{total}).

Mesh level	N_c	N_r	N_t	N_{total}
Coarse	12	15	180	32 400
Medium	25	30	180	135 000
Fine	50	85	180	765 000

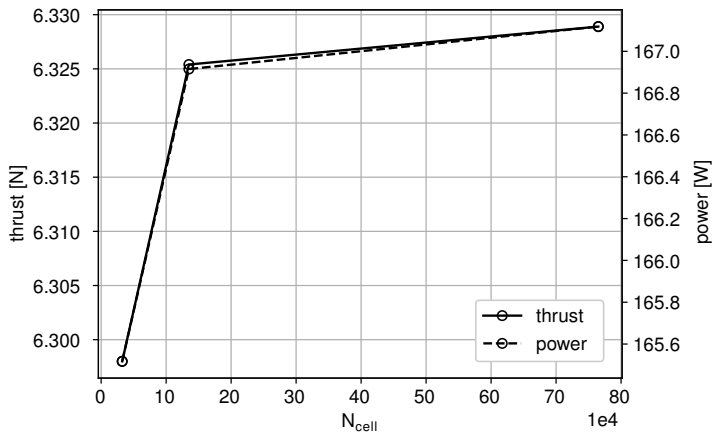

Figure 20: Grid convergence of propeller thrust and shaft power.